In-cycle evolution of thickness and roughness parameters during oxygen plasma enhanced ZnO atomic layer deposition using *in situ* spectroscopic ellipsometry \odot

Special Collection: Atomic Layer Deposition (ALD)

Yousra Traouli [0]; Ufuk Kilic [0]; Sema G. Kilic [0]; Matthew Hilfiker [0]; Daniel Schmidt [0]; Stefan Schoeche; Eva Schubert [0]; Mathias Schubert [0]



J. Vac. Sci. Technol. A 42, 052403 (2024)

https://doi.org/10.1116/6.0003830





20 September 2024 16:02:04



In-cycle evolution of thickness and roughness parameters during oxygen plasma enhanced ZnO atomic layer deposition using in situ spectroscopic ellipsometry

Cite as: J. Vac. Sci. Technol. A 42, 052403 (2024); doi: 10.1116/6.0003830 Submitted: 13 June 2024 · Accepted: 15 August 2024 · Published Online: 6 September 2024







Yousra Traouli, ^{1,a)} 🕩 Ufuk Kilic, ^{1,b)} 🕩 Sema G. Kilic, ¹ 🕩 Matthew Hilfiker, ¹ 🕩 Daniel Schmidt, ² 🕩 Stefan Schoeche, ³

AFFILIATIONS

- Department of Electrical and Computer Engineering, University of Nebraska-Lincoln, Lincoln, Nebraska 68588
- ²IBM Research, 257 Fuller Rd, Albany, New York 12203
- ³J.A. Woollam Co., Inc., Lincoln, Nebraska 68508

Note: This paper is part of the 2025 Special Topic Collection on Atomic Layer Deposition (ALD).

We investigate the time evolution of ZnO thin film growth in oxygen plasma-enhanced atomic layer deposition using *in situ* spectroscopic ellipsometry. The recently proposed dynamic-dual-box-model approach [Kilic *et al.*, Sci. Rep. 10, 10392 (2020)] is used to analyze the spectroscopic data post-growth. With the help of this model, we explore the in-cycle surface modifications and reveal the by-layer growth and surface roughness modification mechanisms during the ZnO ultrathin film dielectric function of the amorphous ZnO thin film is also determined from the tric function is analyzed using a critical point model addition to the index of refraction where the where the surface roughness changes due to nucleation and island growth prior to film coalescence, which then lead to the surface conformal layer-by-layer growth with constant surface roughness. The thickness evolution is resolved with Angstrom-scale resolution vs time. We propose this method for fast development of growth recipes from real-time in situ data analysis. We also present and discuss results from x-ray diffraction, x-ray photoelectron spectroscopy, and atomic force microscopy to examine crystallographic, chemical, and morphological characteristics of the ZnO film.

Published under an exclusive license by the AVS. https://doi.org/10.1116/6.0003830

I. INTRODUCTION

Transition metal oxides are of general interest for broad ranges of practical applications, for example, in electronics, 1energy harvesting,⁴⁻⁶ pharmacology,⁷⁻¹⁰ and many more. Zinc oxide (ZnO) is well known and well investigated for its numerous appeals in materials sciences as well as life sciences. For example, ZnO is highly appealing due to its wide direct bandgap energy

 $(\approx 3.3 \text{ eV})$, 11,12 which lends itself as a suitable material for use in photodetectors, 13,14 light-emitting devices, 15 and laser diodes. 2 More recently, ZnO has regained attraction due to its potential use in quantum technologies as a prospective host for quantum emitters and quantum information storage. 16 Its excellent thermal conductivity makes ZnO suitable for high-power amplification and self-heating devices.¹⁷ The bandgap of ZnO can be varied by choice of growth conditions, e.g., temperature, as well as by alloying with

⁴NanoLund and Solid State Physics, Lund University, 22100 Lund, Sweden



other metal oxides including but not limited to aluminum oxide and magnesium oxide, 18,19 vastly expanding its potential in the aforementioned applications. Additionally, ZnO possesses a large high order nonlinear susceptibility. The second and third-order nonlinear optical coefficients are particularly critical for integrated nonlinear optical devices. 20,21 Because of its pronounced near-band edge luminescence ability, thin film and nanostructured forms of ZnO have recently been employed in single photon emission processes, ²² quantum emitter systems, ²³ and biomedical imaging applications. ²⁴ It has been experimentally realized that ZnO is extremely sensitive to several gas species such as ammonia and hydrogen allowing it to be a superb material for gas sensors. 25,26 The potential of photocatalytic activity of ZnO broadens its scope in solar cells and lithium-ion batteries.²³

With the ever-increasing research focus on the development of nanotechnology, the precise control of the material growth characteristics is crucial. Reducing a bulk material to the nanoscale unlocks unique structural, electrical, chemical, or mechanical properties.^{29,30} For example, the bulk form of ZnO normally exhibits a white and opaque behavior, however, it turns clear and transparent at the nanoscale.³¹ Multiple deposition techniques for the fabrication of ZnO thin films have been established such as magnetron sputtering,³² pulsed laser deposition,^{33,34} electron beam evaporation,³⁵ molecular beam epitaxy,³⁶ and chemical deposition (e.g., spray pyrolysis and sol–gel).^{37,38} However, some of these methods suffer from limitations such as poor conformality, nonuniformity, and reduced compositional control.^{39,40} Within the last decades, another deposition technique the so-called atomic layer deposition (ALD), which provides thin films with suppressed roughness, extraordinary uniformity, and conformal surface overgrowth capability has garnered remarkable attention in many fields including photonics, optics, and biology. 41-43 More specifically, the ALD technique paves the way for the development of versatile complex nanostructure and multilayer thin film systems. 44 Its unique nanoscale conformal coating ability over various photonic, electronic, and magnetic structures with high aspect-ratio features also can prevent post-fabrication material degradation and, therefore, the extension of tech longevity. 44-49 For ultrathin films, ALD, which generally requires high temperature growth processes, results in increased roughness and often leads to the occurrence of pinholes. Reducing the temperature then leads the incoming precursor material to a condensation process with insufficient surface energy activation.⁵⁰ The integration of a plasma process into ALD is often referred to as plasma-enhanced atomic layer deposition (PE-ALD), which has been proposed as a potential remedy for the aforelisted shortcomings. The benefit of producing highly energetic reactive species such as electrons, ions, and radicals during the reactant exposure step can offer a highly diverse but selective reactivity to a surface without the use of heat.⁵¹ Hence, with PE-ALD process, the lower substrate temperature offers an increase in the film density. 52,53 To maximize the self-limiting behavior, a careful optimization of the process conditions (such as temperature, pressure, pulse time, and selection of precursor/reactant) is needed.⁵⁴ This series of systematic activity determines ALD process parameters or the so-called ALD-window.

To control the growth, it is essential to characterize the intricate processes that take place during the cyclic exposure of

precursors to the surface. Establishing the relationship between atomic-scale dynamic mechanisms and the final fabricated film at the end of each ALD cycle necessitates the employment of reliable characterization techniques. Spectroscopic ellipsometry (SE) is a widely accepted real-time growth monitoring method known for its contact-free and noninvasiveness with subangstrom layer-thickness resolution capability. 55-57 Hence, SE is an excellent tool for investigating the material-surface interaction during the ALD process. Multiple reports exist of the thickness evolution of ZnO thin films by cycle number obtained through in situ SE. 58-61 Skopin et al., using in situ SE, studied the ZnO ALD growth on InGaAs substrates and monitored the ZnO film thickness, disregarding the effects of the interface or roughness layers. The authors reported the influence of the Zn precursor (diethylzinc) and oxidant (water) injection time (the concentration of ZnO initial growth stages) on the substrate.⁵⁸ Macco et al. reported in situ SE measurements for temporal and spatial ALD of Al-doped ZnO thin films.⁵⁹ Mameli et al. performed in situ ellipsometry analysis of area-selective ALD of ZnO thin films. In addition, the nucleation delays were also studied in detail as a function of growth temperature. Details of the optical model layer structure used for in situ SE were not provided.⁶⁰ Demelius et al. measured PE-ALD of ZnO thin films deposited onto polymer and silicon surfaces. A single-box model optical model layer was used for in situ SE data reduction. 61 Ex situ SE measurements were also examined by Knoops et al. 62 and Elam et al. 63 Knoops et al. extracted the room-temperature dielectric function of plasma-deposited ZnO thin films in the infrared to ultraviolet spectral range.⁶² Elam et al. reported ex situ ellipsometry investigations of ALD ZnO thin films as a function of the ALD cycle number and growth temperature. The surface roughness at the end of each deposition was determined ex situ from atomic force microscopy measurements. The evolution of the total & attached mass was monitored by quartz crystal microbalance, of which does not permit differentiation between thickness and roughness evolution.⁶³ Iqbal et al. focused on achieving the highest possible rate of growth (0.56 nm per cycle at a substrate temperature of 200 °C) of ZnO thin films deposited by ALD at different substrate temperatures (from 100 °C to 300 °C) and associated modifications on the thickness and energy bandgap.⁶⁴ Zhao et al. employed the spatial ALD technique, which enables the deposition of thin films with spatial control over their distribution on a substrate, to prepare ZnO thin films with high transparency and crystallinity in the low temperature range from 55 to 135 °C.65 Bohorquez et al. presented the ellipsometry analysis of thermal ALD thin films of ZnO doped with zirconium (Zr) onto several substrates. The authors investigated the effect of the post-growth temperature annealing (ranging from 100-300 °C) on the bandgap.66 A recently proposed dynamic dual box model developed by Kilic et al. for in situ SE data analysis allows for resolving the in-cycle evolution of both thin films and void fraction rate in the chemical interface layer at the surface for various transition metal oxide ALD processes.⁶⁷ In summary, SE based thickness monitoring of ALD processes for different transition metal oxides including ZnO has been previously reported.⁶⁸⁻⁷¹ However, to the best of our knowledge, a simultaneous analysis of the evolution of thickness and surface ligand chemical interface layer roughness during ALD cycles was not performed using in situ SE to identify



cyclic surface modifications in real time PE-ALD growth of ZnO ultrathin films.

In this study, in situ SE data are collected for the spectral range from near infrared (1.7 eV) to near ultraviolet (4.0 eV) with ≈2.5 s time resolution during PE-ALD of ZnO ultrathin film growth. In the analysis of acquired in situ SE data, we utilize a recently developed dynamic dual box model approach to unravel the surface growth characteristics during each PE-ALD cycle of precursor introduction and oxygen plasma treatment.⁶⁷ As a fundamental input of this simplistic model framework, the ZnO in situ complex dielectric function spectrum is successfully extracted by using the multisample analysis approach (MSA). Hence, with this model approach, we are able to (i) trace the interactions from sequential surface chemical processes at the growth front and (ii) reveal the cyclic surface modifications during the deposition of ZnO ultrathin films. By using a critical point model dielectric function analysis, we determined the band-to-band transitions near the bandgap region. Complementary x-ray photoelectron spectroscopy (XPS), x-ray diffraction (XRD), and atomic force microscopy (AFM) are also used to provide the compositional, structural, and morphological characteristics of the ZnO films, respectively.

II. EXPERIMENTAL AND MEASUREMENT DETAILS

Plasma-enhanced atomic layer deposition: A commercially available Fiji F200 (Veeco CNT) apparatus was utilized to perform PE-ALD of ZnO thin films. The (100) oriented wafers with native oxide were cut from low-B-doped, p-type conductive, single crystalline silicon. Figure 1(a) depicts the schematic representation of the full recipe of the ZnO ALD cycle. The recipe for ZnO thin film consists of two main steps: (i) prior to the deposition and (ii) during the deposition processes. In the first step, an oxygen plasma (300 W) cleaning was applied for 30 min to the sample to remove the impurities and contaminants from the surface. The reactor chamber was then given a stabilization period to allow it to attain a steady state temperature. In the second step, the cycle-by-cycle growth mechanism of ZnO ALD has four main stages. The first stage was using a reactant precursor diethylzinc

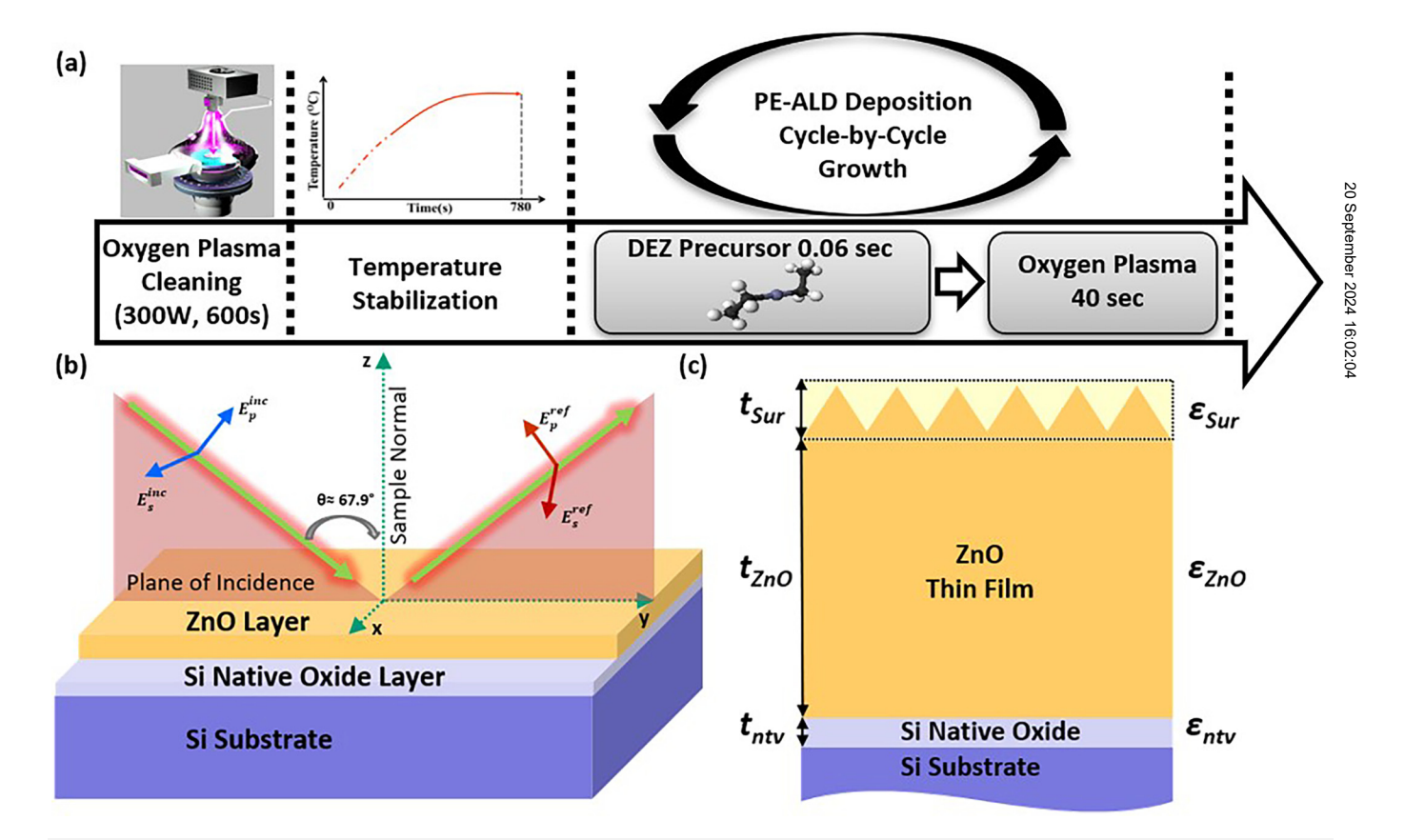


FIG. 1. (a) Predeposition processes that include both plasma cleaning and temperature stabilization (at 250 °C) along with the details of ZnO ALD single cycle are schematically represented. (b) The working mechanism of reflection mode spectroscopic ellipsometry (SE). SE detector and light source ports are mounted on the ALD instrument with 67.9°. (c) Schematic representation of the ellipsometry model so-called dynamic dual box model involves five substances in total: substrate, native oxide layer with thickness t_{ntv} , ZnO thin film layer with thickness t_{ZnO} , surface ligand layer with thickness t_{Sur} and $\varepsilon_{\text{Sur}} = \varepsilon_{\text{ZnO}} (1 - f_{\text{Void}}) + f_{\text{Void}}$, and ambient (Ref. 67). Two of these parameters were employed as dynamic parameters: t_{ZnO} and f_{Void} .



TABLE I. PE-ALD deposition parameters of the ZnO ultrathin film.

Stage	DEZ pulse (s)	Oxygen flow (SCCM)	Oxygen plasma pulse (s)	Argon flow (SCCM)	Argon plasma flow (SCCM)	Chamber pressure (Torr)
I	ON (0.06 s)	0	OFF	40	200	0.27
II	OFF	0	OFF	40	200	0.23
III	OFF	30	ON (40 s)	40	200	0.25
IV	OFF	0	OFF	40	200	0.23

(DEZ) ((C₂H₅)₂Zn) for 0.06 s. The second and fourth stages were argon purging mechanisms to prevent both the reactions between the two precursors and the adverse impacts on the uniformity of the deposited films. The third stage was applying a co-reactant precursor oxygen plasma for 40 s. Table I shows the deposition parameters of the ZnO ALD process.

In situ spectroscopic ellipsometry: The ratio of the sample reflectivity for parallel-polarized light (rp) over the sample reflectivity for perpendicular-polarized light (r_s) can be utilized to determine the change in the polarization state. This ratio is a complex number ρ frequently expressed in terms of the ellipsometric measurements Ψ (amplitude ratio) and Δ (phase difference) which are determined by the equation below:

$$\rho = \frac{r_p}{r_s} = \tan{(\Psi)}e^{i\Delta}.$$
 (1)

A simplistic working principle of the SE technique is depicted in Fig. 1(b). In this study, a rotating compensator SE instrument (M2000S, J. A. Woollam Co., Inc.) was mounted to the ALD reactor chamber at a fixed angle of incidence at 67.9°, and the in situ SE data were acquired from 1.7 to 4 eV. In order to prevent any stress-related polarization changes, strain-free fused silica port windows were used, and the effects of vacuum port windows were taken into account prior to in situ SE data analysis.

Atomic force microscopy: The ZnO thin film samples were examined using a multimode AFM instrument (Bruker-Nanoscope III). The AFM image is analyzed using Nanoscope Visualization and Analysis software.

X-ray diffraction: Cu- K_{α} radiation was used to conduct the measurements of XRD with a Rigaku SmartLab diffractometer.

X-ray photoelectron spectroscopy: In an ultrahigh vacuum (UHV) chamber at about 10⁻¹⁰ Torr, XPS spectra were collected using a dual anode x-ray source and a hemispherical angle-resolved electron analyzer (detector). The Mg-K α line at 1253.6 eV was employed as the x-ray source, and the data were acquired during normal emission.

III. RESULTS AND DISCUSSION

Figure 1(c) shows a schematic illustration of the dynamic dual box model utilized to analyze the acquired in situ SE data. This simplistic model consists of five components: substrate, mixed native oxide and roughness interface layer, metal oxide thin film layer, surface ligand layer, and ambient. Two parameters, the ZnO ultrathin film layer thickness t_{ZnO} and the surface ligand layer void

fraction f_{Void} , are considered dynamic parameters in the best match model calculations of our in situ SE data. The surface ligand layer describes the effect of an ultrathin surface roughness layer, which contains contributions from geometrical roughness as well as surface ligands. This layer must be understood within the so-called ultrathin film limit. It was shown by Rodenhausen et al. that the thickness and dielectric function of such ultra thin surface layers cannot be differentiated by ellipsometry.⁷² Hence, one of these two information must be known a priori for data analysis. It was further shown that no depth gradient information about the inner structure of such layers, e.g., in porous organic surfactant layers, can be obtained. As a result, it was also shown that the effective dielectric function of rough surface layers with multiple constituents and in the ultra thin film limit can be obtained by the linear effective medium approximation. Then, either the thickness, here $t_{
m Sur}$, or the dielectric function, here $arepsilon_{
m Sur}$ can be obtained. $arepsilon_{
m Sur}$ can be replaced as a parameter by fraction f_{Void} if the dielectric function of the ZnO constituent and the void are known. We assume here that after any given ALD cycle, the ZnO material deposited can be described by the same dielectric function. The same assumption was made previously for other metal oxide thin films grown by ALD. Hence, the dielectric function in the ZnO thin film model layer, $\varepsilon_{\rm ZnO}$, and for the ZnO constituent of the surface ligand layer $\stackrel{\aleph}{\sim}$ are considered to be the same. An effective medium approach for the dielectric function of the surface ligand layer is implemented as a linear relationship between the dielectric function of the ambient, $\varepsilon_a=$ 1, and the dielectric function of ZnO, ε_{ZnO} , with the unfilled volume fraction, f_{Void} , $\varepsilon_{\text{Sur}} = \varepsilon_{\text{ZnO}} (1 - f_{\text{Void}}) + f_{\text{Void}}$. Here, we chose $t_{Sur} = 1.92 \text{ nm}$, which is equal to the scan-area-averaged peak-to-valley distance obtained from AFM surface scans, which were performed ex situ after the ALD growth (Fig. 4). The dielectric function for the silicon substrate at the growth temperature was obtained from the software package database provided by J. A. Woollam Co. Inc., which was determined from a similar boron doped silicon substrate previously. 73,74 The dielectric function of the native oxide layer utilized in our model approach was taken from Herzinger et al. 73 The native oxide layer thickness, t_{ntv}, is obtained by using ex situ multiple angle of incidence SE data prior to the deposition, and it is found at 1.77 nm for silicon substrates utilized in this study for the growth of 100 ZnO ALD cycles. This simplistic model approach demonstrated its capability of reproducing the spectral and time-dependent behaviors of SE data during each ALD cycle for various transition metal oxides.

In Figs. 2(a) and 2(b), the time evolution of SE parameters Ψ and Δ acquired during 100 ALD cycles of ZnO is displayed relative

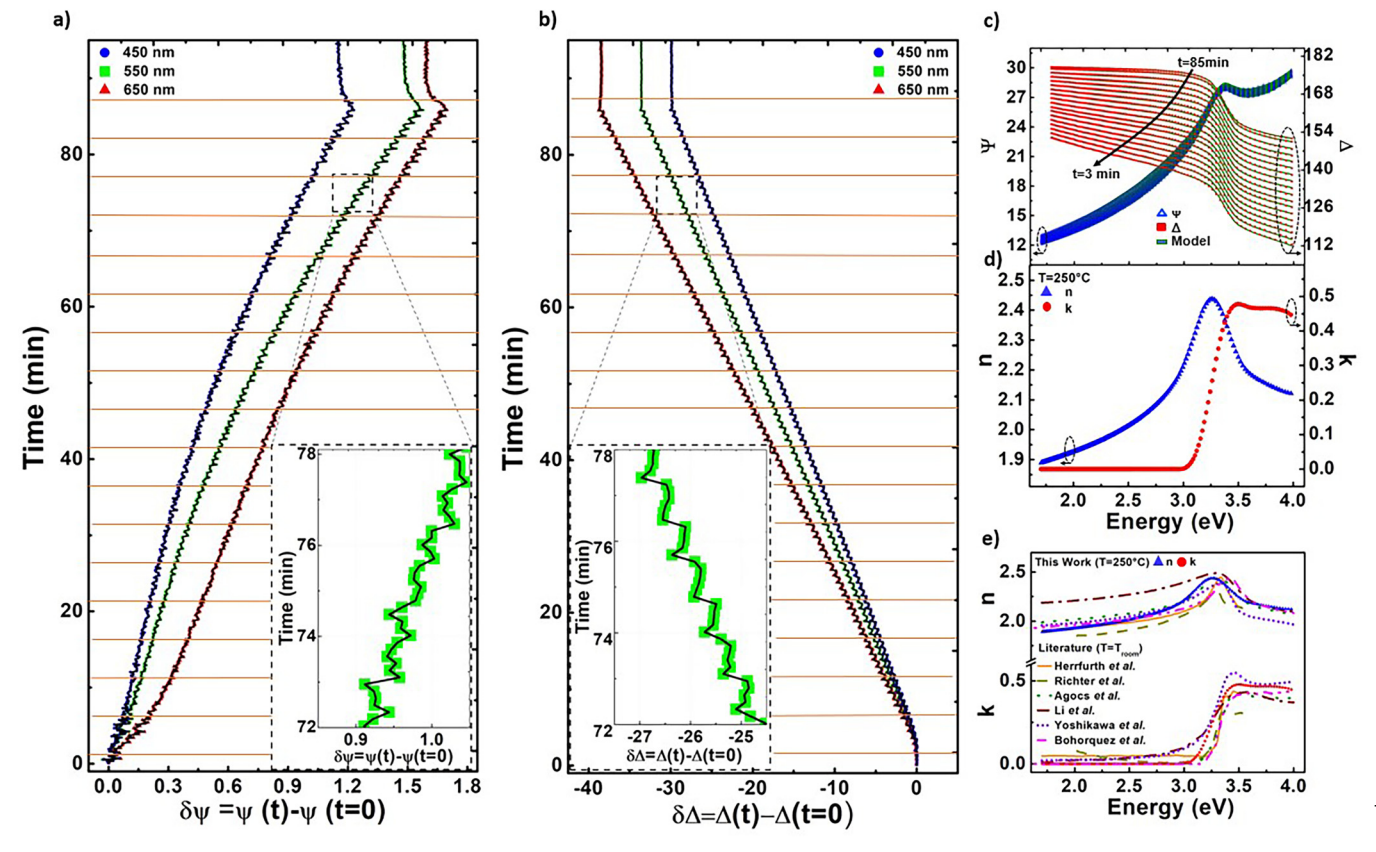


FIG. 2. Time evolution of *in situ* experimental ellipsometry data presented in terms of the change in ψ and change in Δ from their initial conditions at t = 0. (a) $\delta\psi = \psi(t)-\psi(t=0)$ and (b) $\delta\Delta = \Delta(t)-\Delta(t=0)$ at three selected wavelengths: $\lambda = 450$ nm (blue, circles), $\lambda = 550$ nm (green, squares), and $\lambda = 650$ nm (red, triangles) are plotted with their corresponding best-match model calculation results (black solid lines). Inset figures in both (a) and (b) show cyclic oscillations in eight full ALD cycles from the data set of $\lambda = 550$ nm. (c) *In situ* SE data ψ and Δ are shown as a function of energy together with the best-match model analysis results. ψ , Δ , and the model are represented by red squares, blue triangles, and green solid lines, respectively. (d) The best-match model regression analysis results of the refractive index *n* (blue triangles) and extinction coefficient *k* (red circles) of the dielectric function of ZnO ultrathin film using the B-spline function shown in Fig. 3. (e) The refractive index and extinction coefficient of ZnO extracted from the literature (Refs. 66, 75, 76, 77, 78 and 79) are included for comparison.

to the start of the ALD process (t=0) that are given as $\delta \Psi = \Psi(t) - \Psi(t=0)$ and $\delta \Delta = \Delta(t) - \Delta(t=0)$ for three selected wavelengths: 450 nm (blue solid circle symbol), 550 nm (green solid square symbol), and 650 nm (red solid triangle symbol). From Figs. 2(a) and 2(b), we found that the change in $\delta\Delta(t)$ is approximately one order of magnitude larger than the change in $\delta \Psi(t)$. Overall, the time evolution of $\delta\Delta(t)$ [see Fig. 2(b)] is significantly linear, which is indicative of the same amount of material addition per each ALD cycle. Moreover, we can clearly observe monotonous oscillation patterns in $\delta\Delta(t)$ [see the inset in Fig. 2(b)], which stems from the cyclic nature of the ALD process. On the other hand, we observe relatively smaller change in Ψ [see the inset in Fig. 2(a)] as compared to the change in Δ , which is mostly attributed to a slight variation in the light absorption of thin films due to the material addition within each of the ALD cycles. While we can observe the trace of cyclic surface modifications on both Ψ and Δ, the indirect optical characterization nature of SE technique necessitates to have a model approach to access the optical and structural properties of the ZnO ultrathin film.

As previously mentioned, we employ the dual box model approach that introduces $t_{\rm ZnO}$ and $f_{\rm Void}$ as the dynamic variables (i.e., evolving in time during the deposition). Thereby, in the fit process of these dynamic variables, the other parameters are considered static and are listed as follows (i) the dielectric function of ZnO $\varepsilon_{\rm ZnO}$, (ii) native oxide layer thickness $t_{\rm ntv}$, and (iii) roughness layer thickness $t_{\rm Sur}$. With this approach, the potential correlation between the parameters employed in our proposed model is also suppressed.

To derive the ZnO optical constants, we employed the widely used multiple sample analysis (MSA) technique, leveraging SE data obtained from multiple thin film samples with varying thicknesses but deposited under identical conditions. ^{80–82} In contrast to the conventional MSA technique reliant on *ex situ* SE measurements, we introduced MSA based on *in situ* SE data of ZnO thin films,

marking the first application of this approach for ZnO ALD, to the best of our knowledge. Given the consistent material growth facilitated by ALD processes, we simultaneously perform the analysis of 18 individual time slices from *in situ* SE data obtained at the end of arbitrarily selected ALD cycles [see Fig. 2(c) for Ψ (red square symbol) and Δ (green triangle symbol) spectra inlaid with the model (solid dark green line) results]. Figure 2(d) illustrates the n and k of a ZnO ultrathin film deposited at 250 °C. Additionally, for comparative purposes, Fig. 2(e) incorporates n and k of ZnO films sourced from existing literature $^{66,75-79}$ in order to compare with the one that is obtained from our *in situ* SE data within the MSA approach.

Figure 3 displays the optical constants of ZnO, which were determined using a B-spline function for ε_2 (blue hollow circles), where the real component ε_1 (red hollow triangles) was determined through the Kramers–Kronig relationship.⁸³

$$\varepsilon_1(E) = \frac{2}{\pi} P \int_0^\infty \frac{\xi \varepsilon_2(\xi)}{\xi^2 - E^2} d\xi.$$
 (2)

This provides an excellent model fit across the full spectral range, for all selected (Ψ, Δ) time slices. Alternatively, the dielectric function maybe determined using a wavelength-by-wavelength approach. However, the B-spline function approach was selected here because it permits to reduce parameter correlation which is helpful when analyzing ellipsometry data from ultrathin films. 83

In order to unravel the band-to-band transitions within the near bandgap region, a critical point (CP) model dielectric function (MDF) is employed by taking the B-spline dielectric function as a reference. The dielectric function of semiconductors is

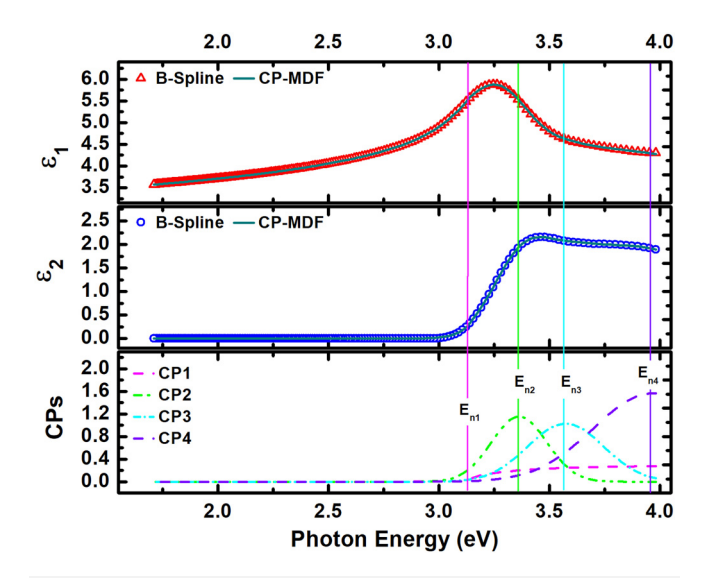


FIG. 3. Real (ε_1) and imaginary (ε_2) parts of the ZnO dielectric function acquired by B-spline analysis (red hollow triangles and blue hollow circles, respectively) and by CP-MDF analysis (dark cyan solid lines). The bottom section displays the individual CP contributions. The vertical line shows the MDF energy parameters listed in Table II.

characterized by contributions from band-to-band transitions at various points within their electronic band structure. The CPs are associated with singularities within the combined density of states. The resulting contributions to the dielectric polarizability are often referred to as CP structures. Each such CP structure can be approximated by physical model lineshape functions. Typical functions are complex-valued and Kramers–Kronig integral-consistent Lorentzian or Gaussian oscillator lineshapes. The sum of their contributions can then be used to render the spectral behavior of the dielectric function within a photon energy region wherein experimental data are available. Here, the complex dielectric function is expressed as a sum over five terms,

$$\varepsilon = \varepsilon_1 + i\varepsilon_2 = \varepsilon_\infty + \sum_{j=1}^4 \varepsilon^{\text{CP}j}(A_j, B_j, E_{nj}, E), \tag{3}$$

where ε_{∞} is a real valued constant to account for a spectral independent offset in the real part of the MDF. Terms $\varepsilon^{\text{CP}j}(A_j, B_j, E_{nj}, E)$ are individual functions for CP structure j $(j=1,\ldots,4)$, characterized by CP amplitude, CP broadening, CP transition energy, and photon energy, respectively, A_j , B_j , E_{nj} , and $E=\hbar\omega$ (\hbar is the Planck constant and ω is the orbital frequency). The CP associated with the bandgap energy (j=1) is represented by the model function for a M_0 -type Van Hove singularity, 85

$$\varepsilon^{\text{CP1}}(E) = \frac{A}{E_{\sigma}^{\frac{3}{2}} \chi^{2}} [2 - \sqrt{1 + \chi} - \sqrt{1 - \chi}], \tag{4}$$

where $\chi = (E + iB)/E_n$. This function is used to display the lineshape of the lowest energy critical point structure. In the dielectric function, for higher energy electronic transitions, three Gaussian oscillators ($\varepsilon^{\text{CP}j}$, j = 2, 3, 4) were employed, ⁸⁶

$$\varepsilon_2^{\text{CP}j}(E) = A_j e^{-\left(\frac{E - E_{\text{n}j}}{\sigma_i}\right)^2} - A_j e^{-\left(\frac{E + E_{\text{n}j}}{\sigma_i}\right)^2}, \tag{5}$$

where $\sigma_j = B_j/2\sqrt{\ln(2)}$. The MDF functions for the real parts, $\varepsilon_1^{\text{CP}j}(E)$, are obtained by Kramers–Kronig integration using Eq. (2). The best-match parameters are detailed in Table II. The CP-MDF is in excellent agreement with the B-spline determined dielectric function. The extracted bandgap value of the ZnO ultrathin film at

TABLE II. CP-MDF amplitude (A_j) , broadening (B_j) , and transition energy $(E_{\eta j})$ parameters for CPj contribution $\varepsilon^{\text{CP}j}$ (j=1,...,4) determined in this work. The constant offset was determined as $\varepsilon_\infty=2.0(2)$. The brackets indicate the last trustworthy digit according to the 90% confidence interval.

CPj,		B_i	E_{ni}	
<u>j</u>	A_{j}	(eV)	(eV)	Equation
1	$4.72(2) \text{ eV}^{3/2}$	0.00(4)	3.13(2)	(4)
2	1.15(6) eV	0.29(4)	3.36(3)	(5) and (2)
3	1.02(9) eV	0.40(3)	3.57(3)	(5) and (2)
4	1.56(3) eV	0.61(7)	3.96(3)	(5) and (2)

TABLE III. ZnO bandgap energy values obtained from different methods and measured at different temperatures including room temperature (RT). The bandgap value determined in this work was obtained from a model dielectric function line shape analysis.

Fabrication	Method	Operation mode	Temperature	Egap (eV)	Reference
PE-ALD	Spectroscopic ellipsometry	In situ	250 °C	3.13	This work
Sol-gel	UV-Vis-NIR spectroscopy	Ex situ	300 °C	3.33	87
	Electron energy-loss spectroscopy	Ex situ	602 °C	3.06	88
Pulsed laser deposition	Temperature dependent spectroscopic ellipsometry	Ex situ	77 °C	3.84	89
Electrodeposition	Spectrophotometry	Ex situ	RT	3.25	90
Chemical vapor deposition	Transmission and reflectance spectrophotometry	Ex situ	RT	3.25	91

250 °C is listed together with the other bandgap values from the literature for comparison in Table III.

ZnO is a Transparent Conductive Oxide (TCO) and conductivity can be controlled by doping. Intrinsic defects like oxygen vacancies and zinc interstitials, which act as donor states introducing free electrons into the conduction band can also contribute to electrical conductivity in undoped ZnO. 92,93 The presence of free charge carriers in semiconductor materials can be revealed by optical experiments such as ellipsometry. The free charge carriers cause modifications to the dielectric function, which are often described by the Drude model. According to this model, free charge carriers cause negative normal dispersion contributions to the real part of the dielectric function in the below bandgap spectral range. The effect increases toward long wavelengths and also increases with increasing carrier density. While our ZnO film is undoped, defects may still cause free charge carriers. However, we did not observe negative normal dispersion in the below bandgap spectral range of our experimental data. Therefore, we did not consider a Drude model contribution for our model dielectric function approach. The exclusion of a Drude model contribution here does not conclude the absence of free charge carriers in our film but instead implies that their density is too low to cause detectable contributions to the optical properties in the spectral range investigated here.

Figure 4(a) shows the time evolution of dynamic parameters $t_{\rm ZnO}$ and $f_{\rm Void}$ in our aforedescribed dynamic dual box model approach, which is obtained by performing the retroactive analysis of in situ SE data acquired during 100 ZnO PE-ALD cycles. We observe that there are two growth regimes prevalent in ZnO in this process: (i) a nonlinear regime (covers the first \approx 15 min, i.e., \approx 20 ALD cycles of the entire ALD process) and (ii) a linear regime (where f_{Void} exhibits a near-constant value with small magnitude modulations on average < 1%). To better understand the behavior of these two dynamic parameters, Fig. 5 displays a schematic representation of the ZnO nucleation process, depicting four steps labeled as A, B, C, and D shown at the same time in Fig. 4(a). Step A shows the beginning of the process when the substrate is ready for precursor introduction. Hence, f_{Void} (indicated by the blue line) is 100% and $t_{\rm ZnO}$ (indicated by the red line) is 0 nm as shown in Fig. 4(a). Moving to step B, the nonlinear regime of the deposition process occurs, 94,95 where we observe deposited species nucleate on the substrate surface, forming small isolated nucleation seeds. While the dynamic parameters display cyclic oscillations resulting from alternating precursor and purging processes, we notice a

decrease in the void fraction occurs (initially at 100%, declining to 85% within 7 min) and $t_{\rm ZnO}$ is still \approx 0 nm. With each deposition cycle, the nucleation grows in size as more atoms are deposited onto the substrate surface. As the deposition process progresses, the neighboring nucleation islands begin to approach each other due to their growth. At a certain point, these islands make contact with each other and merge together gradually covering the entire substrate surface, initiating the coalescence process as it shown in step C. Here, f_{Void} is decreasing (from 85% to 62%), and there is a thickness gain of < 1 nm. Finally, in step D, the coalescence process continues until a continuous and uniform thin film is formed. The ZnO ultrathin film thickness, t_{ZnO} , develops linearly after 20 cycles (≈15 min) as a result of the precursors' self-limited chemical adsorption on a substrate. After 28 cycles (\approx 25 min), f_{Void} saturates at $\approx 57\%$ as the surface modification of precursor introduction and 80 0 oxygen plasma treatment create a uniform film growth. This results in layer-by-layer ZnO conformal growth. Notably, the general 80 1 behavior of the two dynamic parameters [see Fig. 4(a)] are disc. behavior of the two dynamic parameters [see Fig. 4(a)] are distinctly different from each other. At the end of each ALD cycle, a growth per cycle (GPC) is determined. The calculated average GPC & value from the growth of the entire thin film is found here to be approximately 1 Å/cycle for the growth of a ZnO ultrathin film over 100 ALD cycles.

In order to validate the elemental stoichiometry of our fabricated ZnO ultrathin films, the XPS technique was utilized. Due to the use of an Mg-K_α X-ray line of 1253.6 eV, subsurface regions with a depth of only a few nanometers were probed, preventing the collection of information from areas below ZnO films with a thickness of $t_{ZnO} = 10 \text{ nm.}^{96}$ Fig. 4(b) shows the XPS spectra of (O_{1s}) , $(Zn_{2p1/2})$, and $(Zn_{2p3/2})$ core levels. The measurement depicts that we obtained 52.4% of zinc and 47.6% of oxygen, which is a clear demonstration of near-stoichiometric ZnO thin film fabrication via a PE-ALD process. As another complementary study, the crystallinity of our fabricated ultrathin films is investigated using XRD. Figure 4(c) shows the XRD data for different samples: silicon, silicon/silicon dioxide, silicon/zinc oxide, and silicon/silicon dioxide/zinc oxide. The diffraction peak observed at 35° corresponds to the (002) ZnO peak, associated with the wurtzite crystal-

As it was previously mentioned, the polarization of light allows the SE instrument to be extremely sensitive to surface modifications with subnanometer resolution.⁹⁷ Finally, by examining a single ALD cycle, the evolution of both Ψ and Δ can be associated with the introduction of precursor pulses and O₂ plasma treatment.



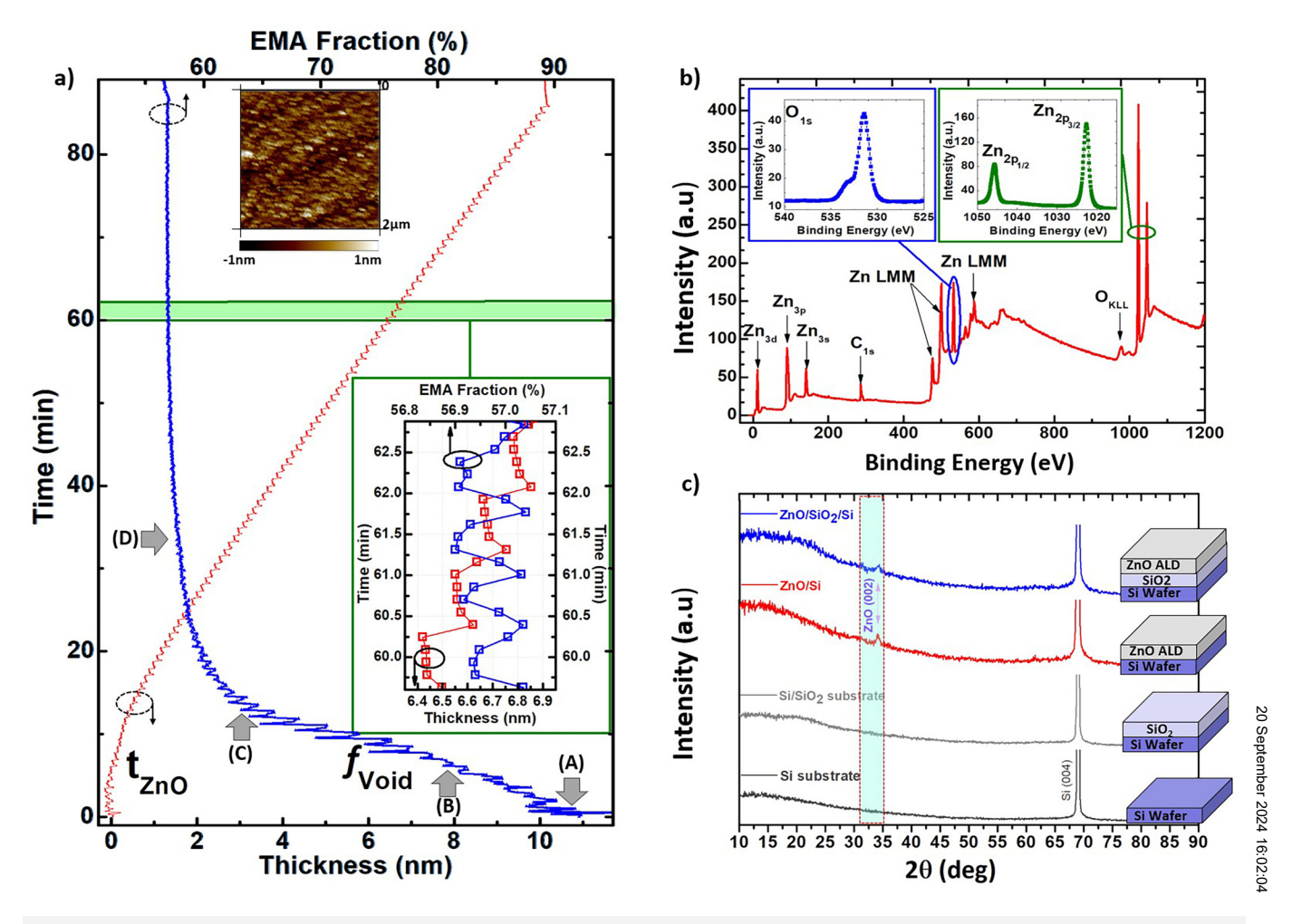


FIG. 4. (a) Parameters for the surface ligand layer void fraction, f_{Void} , and ZnO thin film thickness, t_{ZnO} , represented by blue and red squares, respectively, are determined by the retroactive best-match model calculations based on the dynamic dual box model. A, B, C, and D represent different steps for the ZnO nucleation process (see Fig. 5). AFM imaging was performed after the deposition of 100 cycles of ZnO ALD. The inset shows the evolutions of both t_{ZnO} and f_{Void} throughout the course of four ALD cycles. (b) The resulting XPS survey spectra of the ZnO ALD thin film. The insets display the spectra of O(1s), $Z_{NO}(2p_{1/2})$, and $Z_{NO}(2p_{3/2})$ core levels. A table of deposited ZnO thin film chemical composition percentage is shown. (c) XRD surveys of Si (black), Si/SiO₂ (gray), Si/ZnO (red), and Si/SiO₂/ZnO (blue).

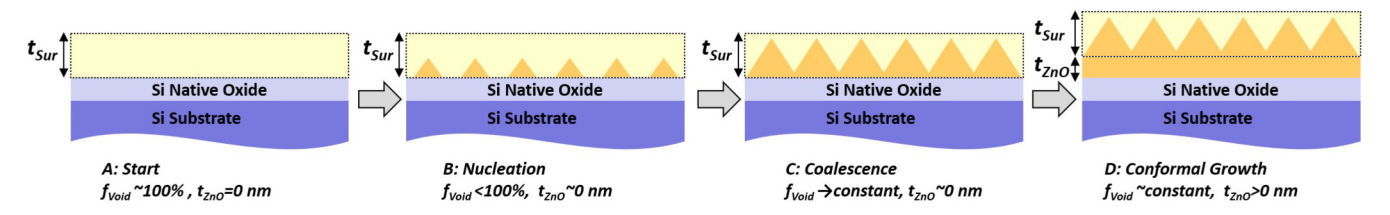


FIG. 5. Schematic presentation the ZnO nucleation process in terms of dynamic parameters in the SE model. (a) At t = 0, no precursor is introduced, hence, f_{Void} is 100% and f_{ZnO} is 0 nm. (b) Small nucleation seeds with an incomplete coverage leads to f_{Void} less than 100% with f_{ZnO} is ≈ 0 nm. (c) As more material is deposited onto the substrate surface during each cycle, the nucleation gradually grows in size. This growth occurs both laterally and vertically. This leads to further decrease in f_{Void} and f_{ZnO} is still ≈ 0 nm. Coalescence occurs as the nucleation sites merge together to form a continuous thin film. At this stage, f_{ZnO} starts increasing while the decrease in f_{Void} slows down. (d) Once coalescence is complete, the thickness gain per each ALD cycle consistently increases f_{ZnO} and f_{Void} remains constant.

The effect of in-cycle ALD growth dynamics for chemical reaction mechanisms on the substrate surface can then be resolved from the standard-mode in situ data acquisition (7 measurements per min). In Fig. 6, the dynamic parameters of the dual box model (t_{ZnO} and f_{Void} , measured SE parameters Ψ and Δ , and the ALD single cycle process steps are overlaid. Thereby, we observe that the dynamic parameters of the dual box model and ALD growth process steps are shown to be directly correlated. The precursor-surface interactions that reoccur cyclically throughout the whole ALD process are now detected by the in situ SE technique and projected into the dynamic thickness (t_{ZnO}) and void fraction f_{Void} parameters. While an increase in thickness and a decrease in void fraction are observed as a response to the introduction of DEZ precursor, a slight reduction of the void fraction, which is attributed to the removal of ligands from the growth surface, is observed during the

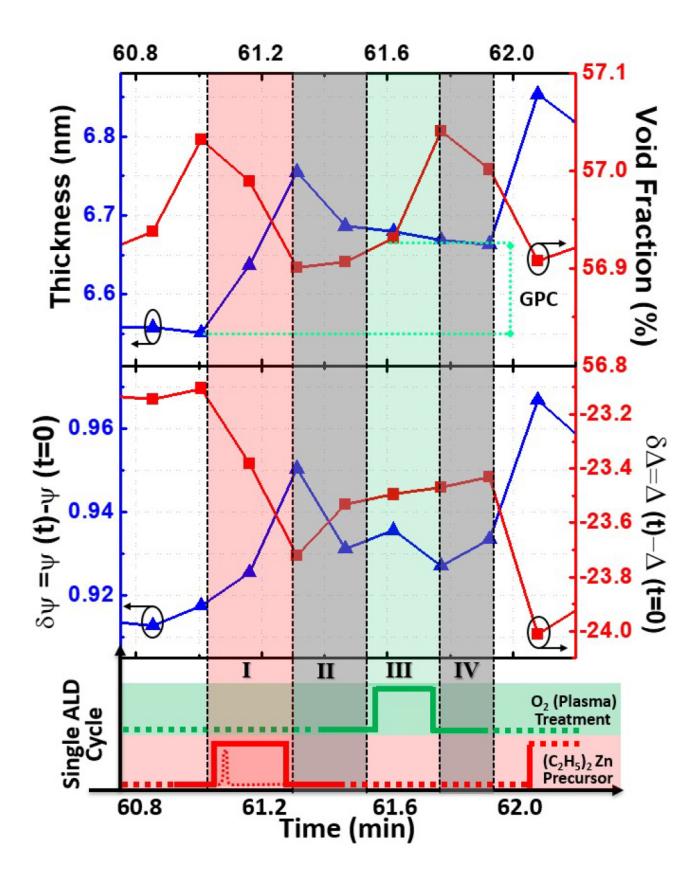


FIG. 6. Dynamic parameters [thickness (blue triangles) and void fraction (red squares)] of dual box model during the course of a single ALD cycle were shown in the top section. The corresponding measured SE data $\delta \psi = \psi(t) - \psi(t)$ (t = 0) (blue triangle symbols) and $\delta\Delta = \Delta(t)-\Delta(t=0)$ (red square symbols) are presented in the mid section. The four main phases within the single cycle are designated by Roman numerals (see Table I) and their sequential pulsing representation were shown in the bottom section. These 4 main phases were also color shaded: the regions labeled II and IV denote periods with argon purging and neighboring cycles are indicated by the white regions to the left and right. GPC thickness is shown by dashed lines.

purging step as well as during the oxygen plasma process. The ALD single cycle process for ZnO thin film fabrication is separated into four distinct phases. During phase I, ((C₂H₅)₂Zn) precursor is introduced. This leads to an increase of t_{ZnO} by approximately 0.2 nm, while the f_{Void} decreases to 56.9% as the precursor attaches to the surface. Phase II is the intermediary step, where the argon purging mechanism occurs. Here, the film stabilizes from the rapid attachment of precursor molecules in the previous phase. This is observed through the dynamic parameters with no change at f_{Void} and a slight decrease in t_{ZnO} (0.6 nm). As a co-reactant precursor, the introduction of O2 plasma in phase III results in a significant increase in f_{Void} to roughly 57.05% as the O₂ modifies the surface to be susceptible to the next $((C_2H_5)_2Zn)$ precursor cycle. Phase IV is the last segment of the ALD cycle where no precursor is added and a secondary purging mechanism is occurring to make the surface ready for the upcoming precursor introduction of the next ALD cycle.

IV. CONCLUSION

In summary, in situ SE is a useful method for elucidating PE-ALD precursor-surface dynamics during ZnO ultrathin film growth. Utilizing a previously reported five-phase dual box model introduced by Kilic et al.⁶⁷ enabled us to obtain an extensive understanding about the intricate ALD growth process and allows us to acquire a reliable in situ PE-ALD recipe. The two dynamic parameters, ZnO ultrathin film thickness, $t_{\rm ZnO}$, and surface ligand layer void fraction, f_{Void} , were examined throughout the four distinct g_{Void} has of the ALD cycle. This allowed for the initial nucleation g_{Void} has been examined throughout the four distinct g_{Void} has been examined g_{Void} and g_{Void} has been examined throughout g_{Void} and g_{Void} has been examined g_{Void} and g_{Void} has bee regimes. This is observed in the ellipsometric model parameters as a rapid decrease in f_{Void} due to the growth of nucleation islands $\frac{8}{8}$ until the end of film coalescence and the beginning of a uniform of layer-by-layer growth regime. The quality of the resulting ultrathin films were verified through XRD and XPS measurements, which confirms the structural and chemical composition of our ZnO film. We also introduced in situ SE based MSA and obtained the complex dielectric function, which plays an essential role in the retroactive analysis of dynamic parameters utilizing the dual box model. The application of critical point model dielectric function analysis disclosed near bandgap band-to-band transitions. The dual box model approach may be useful for similar PE-ALD process characterization.

ACKNOWLEDGMENTS

This work was partially supported by the National Science Foundation (NSF) under Award Nos. ECCS 2329940, DMR 1808715, CMMI 2211858, and OIA-2044049 Emergent Quantum Materials and Technologies (EQUATE), Air Force Office of Scientific Research under Award Nos. FA9550-19-S-0003, FA9550-21-1-0259, and FA9550-23-1-0574 DEF, Nebraska Materials Research Science and Engineering Center under Award No. DMR 1420645. M.S. acknowledges the University of Nebraska Foundation and the J. A. Woollam Foundation for financial support. We appreciate the insightful conversation with Alyssa Mock (Weber State University), Giselle Melendez (Polytechnic



University of Puerto Rico), and Derek Sekora (Honeywell Federal Manufacturing & Technologies, LLC).

AUTHOR DECLARATIONS

Conflict of Interest

The authors have no conflicts to disclose.

Author Contributions

Yousra Traouli: Data curation (equal); Formal analysis (equal); Investigation (equal); Methodology (equal); Writing - original draft (equal). Ufuk Kilic: Data curation (equal); Formal analysis (equal); Investigation (equal); Methodology (equal); Supervision (equal); Writing - original draft (equal); Writing - review & editing (equal). Sema G. Kilic: Formal analysis (supporting); Writing - review & editing (supporting). Matthew Hilfiker: Formal analysis (equal); Investigation (equal); Methodology (equal); Writing - review & editing (equal). Daniel Schmidt: Methodology (equal). Stefan Schoeche: Methodology (equal). Eva **Schubert:** Formal analysis (equal); Funding acquisition (equal); Investigation (equal); Methodology (equal); Resources (equal); Supervision (equal); Writing - review & editing (equal). Mathias Schubert: Data curation (equal); Formal analysis (equal); Investigation (equal); Methodology (equal); Supervision (equal); Validation (equal); Writing – review & editing (equal).

DATA AVAILABILITY

The data that support the findings of this study are available within the article and its supplementary material.

REFERENCES

- ¹A. Magdy, A. El-Shaer, A. El-Farrash, and E. Salim, Sci. Rep. 12, 21489 (2022).
- ²F. Schuster, B. Laumer, R. R. Zamani, C. Magen, J. R. Morante, J. Arbiol, and M. Stutzmann, ACS Nano 8, 4376 (2014).
- ³A. Calzolari, A. Ruini, and A. Catellani, J. Am. Chem. Soc. 133, 5893 (2011).
- ⁴A. Anand and M. Bhatnagar, Mater. Today Energy 13, 293 (2019).
- ⁵K. Žídek, M. Abdellah, K. Zheng, and T. Pullerits, Sci. Rep. 4, 7244 (2014).
- ⁶A. Alexandrov, M. Zvaigzne, D. Lypenko, I. Nabiev, and P. Samokhvalov, Sci. Rep. 10, 7496 (2020).
- ⁷Y. A. Selim, M. A. Azb, I. Ragab, and M. H. M. Abd El-Azim, Sci. Rep. 10,
- ⁸A. Mocanu, G. Isopencu, C. Busuioc, O.-M. Popa, P. Dietrich, and L. Socaciu-Siebert, Sci. Rep. 9, 1 (2019).
- ⁹U. Singh, Z. Saifi, M. Kumar, A. Reimers, S. D. Krishnananda, R. Adelung, and M. Baum, Sci. Rep. 11, 15945 (2021).
- 10 H. Asadzadeh Patehkhor, M. Fattahi, and M. Khosravi-Nikou, Sci. Rep. 11, 1 (2021).
- ¹¹R. Schmidt-Grund, B. Rheinländer, E. M. Kaidashev, M. Lorenz, M. Grundmann, D. Fritsch, M. M. Schubert, H. Schmidt, and C. M. Herzinger, J. Korean Phys. Soc. 53, 88 (2008).
- 12C. Bundesmann, R. Schmidt-Grund, and M. Schubert, in Transparent Conductive Zinc Oxide: Basics and Applications in Thin Film Solar Cells (Springer, New York, 2008), pp. 79-124.
- A. Costas, C. Florica, N. Preda, C. Besleaga, A. Kuncser, and I. Enculescu, Sci. Rep. 12, 6834 (2022).
- 14X. Wang, K. Xu, X. Yan, X. Xiao, C. Aruta, V. Foglietti, Z. Ning, and N. Yang, ACS Appl. Mater. Interfaces 12, 8403 (2020).
- ¹⁵N. Abdullayeva *et al.*, ACS Appl. Nano Mater. **3**, 5881 (2020).

- ¹⁶S. MohammadNejad, P. Nosratkhah, and H. Arab, Quantum Inf. Process. 22, 360 (2023).
- 17X. Wu, J. Lee, V. Varshney, J. L. Wohlwend, A. K. Roy, and T. Luo, Sci. Rep. 6, 1 (2016).
- ¹⁸J. Shin, J. Jeon, and D. Bae, Mater. Lett. **151**, 96 (2015).
- 19 H. M. Mousa, A. Abdal-Hay, M. Bartnikowski, I. M. Mohamed, A. S. Yasin, S. Ivanovski, C. H. Park, and C. S. Kim, ACS Biomater. Sci. Eng. 4, 2169 (2018).
- 20B. Krause, D. Mishra, J. Chen, C. Argyropoulos, and T. Hoang, Adv. Opt. Mater. 10, 2200510 (2022).
- ²¹K. Waszkowska, O. Krupka, O. Kharchenko, V. Figà, V. Smokal, N. Kutsevol, and B. Sahraoui, Appl. Nanosci. 10, 4977 (2020).
- ²²M. Jiang, W. Mao, X. Zhou, C. Kan, and D. Shi, ACS Appl. Mater. Interfaces 11, 11800 (2019).
- ²³M. Zakria, T. T. Huynh, F. C. Ling, S. C. Su, M. R. Phillips, and C. Ton-That, ACS Appl. Nano Mater. 2, 2574 (2019).
- ²⁴J. E. Eixenberger et al., ACS Appl. Mater. Interfaces 11, 24933 (2019).
- 25Y. Tu, C. Kyle, H. Luo, D.-W. Zhang, A. Das, J. Briscoe, S. Dunn, M.-M. Titirici, and S. Krause, ACS Sens. 5, 3568 (2020).
- ²⁶A. Abun, B.-R. Huang, A. Saravanan, D. Kathiravan, and P.-D. Hong, ACS Appl. Nano Mater. 3, 12139 (2020).
- A. Soultati et al., ACS Appl. Mater. Interfaces 12, 21961 (2020).
- 28Y.-Q. Cao, S.-S. Wang, C. Liu, D. Wu, and A.-D. Li, Sci. Rep. 9, 11526 (2019).
- ²⁹S.-K. Jung et al., Chem. Rev. 120, 6684 (2019).
- **30**K. Li et al., ACS Nano **15**, 3646 (2021).
- 31 Y. Gao, I. Gereige, A. El Labban, D. Cha, T. T. Isimjan, and P. M. Beaujuge, ACS Appl. Mater. Interfaces 6, 2219 (2014).
- 32 F. Otieno, M. Airo, R. M. Erasmus, A. Quandt, D. G. Billing, and D. Wamwangi, Sci. Rep. 10, 8557 (2020).
- 33P. Karnati, A. Haque, M. Taufique, and K. Ghosh, Nanomaterials 8, 62 (2018).
- 34S. Heitsch et al., Thin Solid Films 496, 234 (2006).
- 35L. Skowronski, A. Ciesielski, A. Olszewska, R. Szczesny, M. Naparty, M. Trzcinski, and A. Bukaluk, Materials 13, 3510 (2020).
 36Y. Darma, S. Muhammady, Y. N. Hendri, E. Sustini, R. Widita, and K. Takase, Mater Sci. Semicond Process 93, 50 (2019)
- Mater. Sci. Semicond. Process. 93, 50 (2019).
- 37H. Fayaz Rouhi and S. Rozati, Appl. Phys. A 128, 252 (2022).
- 38 A. Ismail, A. Menazea, H. A. Kabary, A. El-Sherbiny, and A. Samy, J. Mol. Struct. 1196, 332 (2019).
- 39 A. Alberti, S. Molinaro, F. La Via, C. Bongiorno, G. Ceriola, and S. Ravesi, Microelectron. Eng. 60, 81 (2002).
- ⁴⁰B.-S. Kim, L. Gil-Escrig, M. Sessolo, and H. J. Bolink, J. Phys. Chem. Lett. 11, 6852 (2020).
- ⁴¹G. N. West, W. Loh, D. Kharas, C. Sorace-Agaskar, K. K. Mehta, J. Sage,
- J. Chiaverini, and R. J. Ram, APL Photonics 4, 026101 (2019).
 M. Motola et al., ACS Appl. Bio Mater. 3, 6447 (2020).
- 43 P. Listewnik, M. Hirsch, P. Struk, M. Weber, M. Bechelany, and M. Jędrzejewska-Szczerska, Nanomaterials 9, 306 (2019).
- ⁴⁴D. Schmidt, E. Schubert, and M. Schubert, Mater. Res. Soc. Symp. Proc. 1409, mrsf11 (2012).
- 45D. Schmidt, E. Schubert, and M. Schubert, Appl. Phys. Lett. 100, 011912 (2012).
- ⁴⁶T. Tynell and M. Karppinen, Semicond. Sci. Technol. **29**, 043001 (2014).
- ⁴⁷M. Rahamim, H. Cohen, and E. Edri, ACS Appl. Mater. Interfaces 13, 49423
- 48 J. Castillo-Saenz, N. Nedev, B. Valdez-Salas, M. Martinez-Puente, F. Aguirre-Tostado, M. Mendivil-Palma, D. Mateos, M. Curiel-Alvarez, O. Perez-Landeros, and E. Martinez-Guerra, J. Mater. Sci.: Mater. Electron. 32, 20274 (2021).
- ⁴⁹B. A. Rorem, T. H. Cho, N. Farjam, J. D. Lenef, K. Barton, N. P. Dasgupta, and L. J. Guo, ACS Appl. Mater. Interfaces 14, 31099 (2022).
- 50R. W. Johnson, A. Hultqvist, and S. F. Bent, Mater. Today 17, 236 (2014).
- 51 H. Profijt, S. Potts, M. Van de Sanden, and W. Kessels, J. Vac. Sci. Technol. A 29, 050801 (2011).
- 52K.-M. Kim, J. S. Jang, S.-G. Yoon, J.-Y. Yun, and N.-K. Chung, Materials 13,

- ⁵³C. Wang, C.-H. Bao, W.-Y. Wu, C.-H. Hsu, M.-J. Zhao, X.-Y. Zhang, S.-Y. Lien, and W.-Z. Zhu, J. Mater. Sci. 57, 12341 (2022).
- ⁵⁴Y. Kim, J.-G. Song, Y. J. Park, G. H. Ryu, S. J. Lee, J. S. Kim, P. J. Jeon, C. W. Lee, W. J. Woo, T. Choi, et al., Sci. Rep. 6, 18754 (2016).
- 55H. Fujiwara, Spectroscopic Ellipsometry: Principles and Applications (Wiley, New York, 2007).
- ⁵⁶C. Sturm, T. Chavdarov, R. Schmidt-Grund, B. Rheinländer, C. Bundesmann, H. Hochmuth, M. Lorenz, M. Schubert, and M. Grundmann, Phys. Status Solidi 5, 1350 (2008).
- ⁵⁷M. Hilfiker *et al.*, Appl. Phys. Lett. **120**, 132105 (2022).
- ⁵⁸E. V. Skopin, J.-L. Deschanvres, and H. Renevier, Phys. Status Solidi A 217, 1900831 (2020).
- ⁵⁹B. Macco *et al.*, Sol. Energy Mater. Sol. Cells **245**, 111869 (2022).
- ⁶⁰A. Mameli, B. Karasulu, M. A. Verheijen, B. Barcones, B. Macco, A. J. Mackus, W. M. E. Kessels, and F. Roozeboom, Chem. Mater. 31, 1250 (2019).
- ⁶¹L. Demelius, M. Blatnik, K. Unger, P. Parlanti, M. Gemmi, and A. M. Coclite, Appl. Surf. Sci. **604**, 154619 (2022).
- ⁶²H. Knoops, B. W. van de Loo, S. Smit, M. V. Ponomarev, J.-W. Weber, K. Sharma, W. M. Kessels, and M. Creatore, J. Vac. Sci. Technol. A 33, 021509 (2015).
- 63 J. Elam, Z. Sechrist, and S. George, Thin Solid Films 414, 43 (2002).
- ⁶⁴J. Iqbal, A. Jilani, P. Z. Hassan, S. Rafique, R. Jafer, and A. A. Alghamdi, J. King Saud Univ. Sci. 28, 347 (2016).
- 65 M.-J. Zhao et al., Nanomaterials 10, 459 (2020).
- ⁶⁶C. Bohórquez, H. Bakkali, J. J. Delgado, E. Blanco, M. Herrera, and M. Domínguez, ACS Appl. Electron. Mater. 4, 925 (2022).
- 67U. Kilic et al., Sci. Rep. 10, 10392 (2020).
- ⁶⁸U. Kumar, C. Feit, S. N. Berriel, A. Arunachalam, T. S. Sakthivel, K. Basu, P. Banerjee, and S. Seal, J. Vac. Sci. Technol. A 39, 060405 (2021).
- 69M. Labbe, K. Cadien, and D. G. Ivey, J. Phys. Chem. C 126, 19883 (2022).
- ⁷⁰M. J. Muller, K. Komander, C. Hohn, R. van de Krol, and A. C. Bronneberg, ACS Appl. Nano Mater. 2, 6277 (2019).
- ⁷¹S. Kim, S.-H. Lee, I. H. Jo, J. Seo, Y.-E. Yoo, and J. H. Kim, Sci. Rep. **12**, 5124 (2022).
- ⁷²K. Rodenhausen and M. Schubert, Thin Solid Films **519**, 2772 (2011).
- ⁷³C. Herzinger, B. Johs, W. McGahan, J. A. Woollam, and W. Paulson, J. Appl. Phys. **83**, 3323 (1998).
- 74M. Hilfiker and N. James, J. A. Woollam Inc., Lincoln, Nebraska 68508, private communication (2024).
- 75S. Richter et al., New J. Phys. 22, 083066 (2020).

- ⁷⁶O. Herrfurth, T. Pflug, M. Olbrich, M. Grundmann, A. Horn, and R. Schmidt-Grund, Appl. Phys. Lett. 115, 212103 (2019).
- ⁷⁷E. Agocs, B. Fodor, B. Pollakowski, B. Beckhoff, A. Nutsch, M. Jank, and P. Petrik, Thin Solid Films 571, 684 (2014).
- ⁷⁸H. Y. H. Yoshikawa and S. A. S. Adachi, Jpn. J. Appl. Phys. **36**, 6237 (1997).
- ⁷⁹X. Li, T. Chen, P. Liu, Y. Liu, Z. Liu, and K. Leong, J. Appl. Phys. **115**, 103512 (2014).
- ⁸⁰U. Kılıç, D. Sekora, A. Mock, R. Korlacki, S. Valloppilly, E. M. Echeverría, N. Ianno, E. Schubert, and M. Schubert, J. Appl. Phys. 124, 115302 (2018).
- ⁸¹J. N. Hilfiker, N. Singh, T. Tiwald, D. Convey, S. M. Smith, J. H. Baker, and H. G. Tompkins, Thin Solid Films 516, 7979 (2008).
- 82 C. Herzinger, P. G. Snyder, F. Celii, Y.-C. Kao, D. Chow, B. Johs, and J. A. Woollam, J. Appl. Phys. 79, 2663 (1996).
- ⁸³J. Mohrmann, T. E. Tiwald, J. S. Hale, J. N. Hilfiker, and A. C. Martin, J. Vac. Sci. Technol. B 38, 014001 (2020).
- 84J. N. Hilfiker and T. Tiwald, Spectroscopic Ellipsometry for Photovoltaics: Volume 1: Fundamental Principles and Solar Cell Characterization (Springer, Cham, 2018), p. 115.
- 85 S. Adachi, Phys. Rev. B 35, 7454 (1987).
- ⁸⁶A. Mock, R. Korlacki, C. Briley, D. Sekora, T. Hofmann, P. Wilson, A. Sinitskii, E. Schubert, and M. Schubert, Appl. Phys. Lett. 108, 051905 (2016).
- 87N. Kamarulzaman, M. F. Kasim, and R. Rusdi, Nanoscale Res. Lett. 10, 1 (2015)
- ⁸⁸C. S. Granerød, A. Galeckas, K. M. Johansen, L. Vines, and Ø. Prytz, J. Appl. Phys. 123, 145111 (2018).
- ⁸⁹R. Kurniawan, I. M. Sutjahja, T. Winata, T. S. Herng, J. Ding, A. Rusydi, and Y. Darma, Opt. Mater. Express 7, 3902 (2017).
- ⁹⁰R. Nedzinskas, A. Suchodolskis, L. Trinkler, G. Krieke, W.-T. Yao, C.-C. Chang, L. Chang, and M. M.-C. Chou, Opt. Mater. 138, 113650 (2023).
- ⁹¹S. D. Ponja, S. Sathasivam, I. P. Parkin, and C. J. Carmalt, Sci. Rep. **10**, 638 (2020).
- 92S. Golovynskyi et al., Vacuum 153, 204 (2018).
 93J. S. Goo, J.-H. Lee, S.-C. Shin, J.-S. Park, and J. W. Shim, J. Mater. Chem. A.
- 6, 23464 (2018).

 94T. Park, J. Lee, J. Park, H. Jeon, H. Jeon, K.-H. Lee, B.-C. Cho, M.-S. Kim, and
- H.-B. Ahn, J. Vac. Sci. Technol. A **30**, 041301 (2012).

 95S.-S. Yim, D.-J. Lee, K.-S. Kim, S.-H. Kim, T.-S. Yoon, and K.-B. Kim, J. Appl.
- Phys. 103, 113509 (2008).
- 96 F. A. Stevie and C. L. Donley, J. Vac. Sci. Technol. A 38, 063204 (2020).
- ⁹⁷M. Losurdo *et al.*, J. Nanoparticle Res. **11**, 1521 (2009).